THE IMPACT OF GAS BULK ROTATION ON THE LYMAN α LINE

Juan N. Garavito-Camargo, Jaime E. Forero-Romero
Departamento de Física, Universidad de los Andes, Cra. 1 No. 18A-10, Edificio Ip, Bogotá, Colombia

AND

Mark Dijkstra
Institute of Theoretical Astrophysics, University of Oslo, Postboks 1029, 0858 Oslo, Norway

ABSTRACT

We present results of radiative transfer calculations to measure the impact of gas bulk rotation on the morphology of the Lyman α emission line in distant galaxies. We model a galaxy as a sphere with an homogeneous mixture of dust and hydrogen at a constant temperature. These spheres have a solid-body rotation with maximum velocities in the range $0 - 300$ km s^{-1}and neutral hydrogen optical depths in the range $\tau_{\rm H} = 10^5 - 10^7$. We consider cases of a single central Lyman α source, and a uniform distribution of sources. Our main result is that rotation introduces a dependence of the line morphology with viewing angle. Observations with a line of sight parallel to the rotation axis yield line morphologies similar to the static case. The greatest difference is observed for lines of sight perpendicular to the rotation axis. In this case the intensity at the line center increases and the line width increase with rotational velocity. For homogeneously distributed sources the line becomes single peaked at rotational velocities larger than half the line width in the static case. Notably, we find that rotation does not not induce any significant spatial anisotropy in the integrated line flux nor in the escape fraction. However, we do find in the homogeneous models a clear increase of the escape fraction with increasing rotational velocity.

Subject headings: galaxies: high-redshift — line: formation — methods: numerical — radiative transfer

1. INTRODUCTION

The detection of strong Lyα emission lines has become an essential method in extra-galactic astronomy to find distant star-forming galaxies (Partridge & Peebles 1967; Rhoads et al. 2000; Gawiser et al. 2007; Koehler et al. 2007; Ouchi et al. 2008; Yamada et al. 2012; Schenker et al. 2012; Finkelstein et al. 2013). The galaxies detected using this method receive the name of Lyα emitters (LAEs). A detailed examination of this galaxy population has diverse implications for galaxy formation, reionization and the large scale structure of the Universe. Attempts to fully exploit the physical information included in the Lyα line require an understanding of all the physical factors involved in shaping the line. Due to the resonant nature of this line, these physical factors notably include temperature, density and bulk velocity field of the neutral Hydrogen in the emitting galaxy and its surroundings.

A basic understanding of the quantitative behavior of the Lyα line has been reached through analytic studies in the case of a static configurations, such as uniform slabs (Adams 1972; Harrington 1973; Neufeld 1990) and uniform spheres (Dijkstra et al. 2006). Analytic studies of configurations including some kind of bulk flow only include the case of a sphere with a Hubble like expansion flow (Loeb & Rybicki 1999).

A more detailed quantitative description of the Lyα line has been reached through Monte Carlo simulations (Auer 1968; Avery & House 1968; Adams 1972). In the last two decades these studies have become pop-

jn.garavito57@uniandes.edu.co
je.forero@uniandes.edu.co
mark.dijkstra@astro.uio.no

ular due to the availability of computing power. Early into the 21st century, the first studies focused on homogeneous and static media (Ahn et al. 2000, 2001; Zheng & Miralda-Escudé 2002). Later on, the effects of clumpy media (Hansen & Oh 2006) and expanding/contracting shell/spherical geometries started to be studied (Verhamme et al. 2006; Dijkstra et al. 2006; Ahn et al. 2014). Similar codes have applied these results to semi-analytic models of galaxy formation (Orsi et al. 2012; Garel et al. 2012) and results of large hydrodynamic simulations (Forero-Romero et al. 2011, 2012; Behrens & Niemeyer 2013). Recently, Monte Carlo codes have also been applied to the results of high resolution hydrodynamic simulations of individual galaxies (Laursen et al. 2009; Barnes et al. 2011; Verhamme et al. 2012; Yajima et al. 2012). Meanwhile, recent developments have been focused on the systematic study of clumpy outflows (Dijkstra & Kramer 2012)and anisotropic velocity configurations (Zheng & Wallace 2013).

The recent studies of galaxies in hydrodynamic simulations (Laursen et al. 2009; Barnes et al. 2011; Verhamme et al. 2012; Yajima et al. 2012) have all shown systematic variations in the Lyα line with the viewing angle. These variations are a complex superposition of anisotropic density configurations (i.e. edge-on vs. face-on view of a galaxy), the inflows observed by gas cooling and the outflows included in the supernova feedback process of the simulation. These bulk flows physically correspond to the circumgalactic and intergalactic medium (CGM and IGM). These effects are starting to be studied in simplified configurations that vary the density and wind characteristics (Zheng & Wallace 2013; Behrens et al. 2014).

However, in all these efforts the effect of rotation, which is an ubiquitous feature in galaxies, has not been systematically studied. The processing of the Lyα photons in a rotating interstellar medium (ISM) must have some kind of impact in the Lyα line morphology.

Performing that study is the main goal of this paper. We investigate for the first time the impact of rotation on the morphology of the Lyα line. We focus on a simplified system: a spherical gas cloud with homogeneous density and solid body rotation, to study the line morphology and the escape fraction in the presence of dust. We base our work on two independent Monte Carlo based radiative transfer codes presented in Forero-Romero et al. (2011) and Dijkstra & Kramer (2012).

This paper is structured as follows: In §2 we present the implementation of bulk rotation into the Monte Carlo codes, paying special attention to coordinate definitions. We also present a short review of how the Lyα radiative transfer codes work and list the different physical parameters in the simulated grid of models. In §3 we present the results of the simulations, with special detail to quantities that show a clear evolution as a function of the sphere rotational velocity. In §4 we discuss the implications of our results. In the last section we present our conclusions.

In this paper we express a photon's frequency in terms of the dimensionless variable $x \equiv (\nu - \nu_a)/\Delta\nu_\alpha$, where $\nu_\alpha = 2.46 \times 10^{15}$ Hz is the Lyα resonance frequency, $\Delta\nu_\alpha \equiv \nu_\alpha\sqrt{2kT/m_pc^2} \equiv \nu_a v_{\rm th}/c$ is the Doppler broadening of the line which depends on the neutral gas temperature T scattering the radiation or equivalently the thermal velocity $v_{\rm th}$ of the atoms. For the temperature $T = 10^4$K used in our radiative transfer calculations the thermal velocity is $v_{\rm th} = 12.8\,{\rm km\,s^{-1}}$.

2. MODELS OF BULK GAS ROTATION

Describing the kinematics of gas rotation in all generality is a complex task, specially at high redshift where there is still missing a thorough observational account of rotation in galaxies beyond $z > 1.0$. Even at low redshifts there is a great variation in the shape of the rotation curve as observed in HI emission as a function of the distance to the galaxy center. However there are two recurrent features. First, in the central galactic region the velocity increases proportional to the radius, following a solid rotation behavior. Second, beyond a certain radius the rotation curve tends to flatten. An ab-initio description of such realistic rotation curves in simulations depends on having access to the dynamic evolution of all mass components in the galaxy: stars, gas and dark matter. Such level of realism is extremely complex to achieve, specially if one wants to get a systematic description based on statistics of simulated objects.

Following the tradition of studies of Lyα emitting systems, we implement a model with simplified geometry. We assume that the gas is homogeneously distributed in a sphere that rotates as a solid body with constant angular velocity. This simple model will contain only one free parameter: the linear velocity at the sphere's surface, $V_{\rm max}$.

2.1. Detailed Implementation of Rotation

In the Monte Carlo code we define a Cartesian coordinate system to describe the position of each photon.
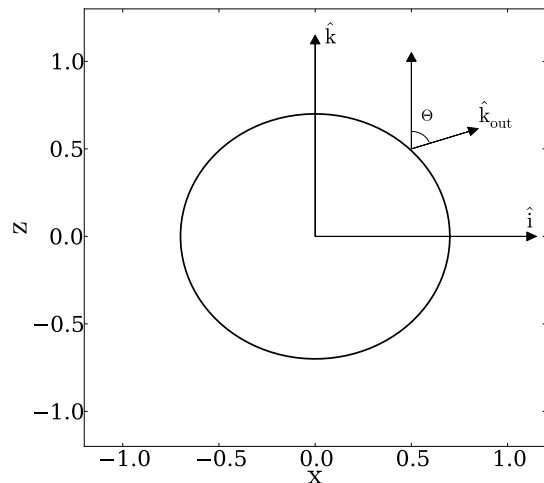

Fig. 1.— Geometry of the gas distribution. The angular velocity vector is parallel to the unit vector $\hat{k}$. In order to describe the departures from spherical symmetry we use the polar angle θ formed by the direction of the outgoing photons with respecto to the z-axis. We define define the variable $\mu \equiv \cos\theta$ to report to present our results. Computing the spectra for photons in a narrow range of μ is equivalent to having a line-of-sight oriented in that direction.

The origin of this system coincides with the center of the sphere and the rotation axis is defined to be z-axis. With this choice, the components of the gas bulk velocity field, $\vec{v} = v_x\hat{i} + v_y\hat{j} + v_z\hat{k}$, can be written as

$$v_x = -\frac{y}{R}V_{\rm max}, \tag{1}$$

$$v_y = \frac{x}{R}V_{\rm max}, \tag{2}$$

$$v_z = 0, \tag{3}$$

where R is the radius of the sphere and $V_{\rm max}$ is the linear velocity at the sphere's surface. The minus/plus sign in the x/y-component of the velocity indicates the direction of rotation. In this case we take the angular velocity in the same direction as the $\hat{k}$ unit vector. With these definitions we can write the norm of the angular velocity as $\omega = V_{\rm max}/R$.

For each photon in the simulation we have its initial position inside the sphere, direction of propagation $\hat{k}_{\rm in}$ and reduced frequency $x_{\rm in}$. The photon's propagation stops once they cross the surface of the sphere. At this point we store the position, the outgoing direction of propagation $\hat{k}_{\rm out}$ and the reduced frequency $x_{\rm out}$. We now define the angle θ by $\cos\theta = \hat{k}_{\rm out} \cdot \hat{k} \equiv \mu$, it is the angle of the outgoing photons with respect to the direction of the angular velocity. We use the variable μ to study the anisotropy induced by rotation. Figure 1 shows the geometry of the problem and the important variables.

2.2. Brief Description of the Radiative Transfer Codes

Here we briefly describe the relevant points for the two radiative transfer codes we have used. For a detailed description we refer the reader to the original papers Forero-Romero et al. (2011); Dijkstra & Kramer (2012).
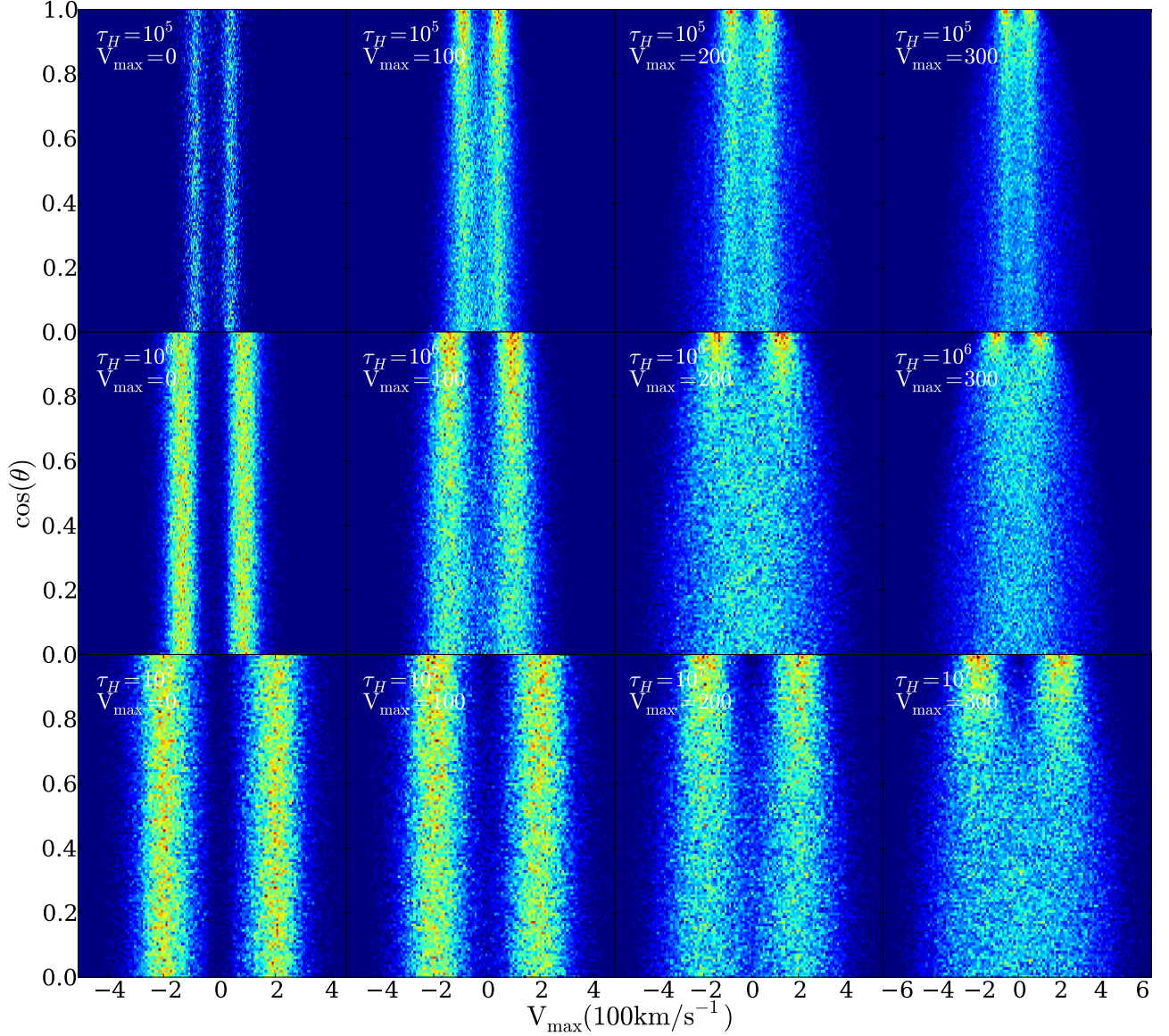
FIG. 2.— 2D histogram showing the number of photons that escape with frecuency x forming an angle θ (parameterized as $|\cos\theta|$) with the rotation axis. The rotational velocity $(0, 100, 200, 300\,\mathrm{km\,s^{-1}})$ increases from left to right and the optical depth (10^5, 10^6, 10^7) from top to bottom. The Lyα photons are initialized at the center of the sphere.

The codes follow the individual scatterings of Lyα photons as they travel through a 3D distribution of neutral Hydrogen. At each scattering the frequency of the photon (in the laboratory frame) and its direction of propagation change. This change in frequency is due to the peculiar velocities of the Hydrogen atom that absorbed and re-emitted the photon. If dust is present, the photon can interact either with a Hydrogen atom or dust grain. In the case of a dust interaction the photon can be either absorbed or scattered, this probability is encoded in the dust albedo, A, which we chose to be $1/2$. In order to obtain accurate values for the escape fraction of photons in the presence of dust, we do not use any accelerating mechanism in the radiative transfer. Once the photons escape the gas distribution we store their direction at their direction of propagation and frequency at their last scattering.

The photons are thus emitted in some region of the gas distribution and follow a random walk in space and frequency until they escape the gas distribution or are absorbed by a dust grain. The initialization process for the Lyα photons has to specify its position, frequency and direction of propagation. In our case we select the initial frequency to be exactly the Lyα rest-frame frequency ($x = 0$) and the direction of propagation to be random following an flat probability distribution over the sphere. A different initization that uses a Gaussian with a velocity with equal to the thermal velocity, $12.8\,\mathrm{km\,s^{-1}}$ in our case, should not introduce noticeable change given that our rotational velocities span the range 100-300 $\mathrm{km\,s^{-1}}$ and the lines have velocity widths on the order of 100-500 $\mathrm{km\,s^{-1}}$.

The gas is completely defined by its geometry (i.e. sphere or slab), temperature T, Hydrogen optical depth
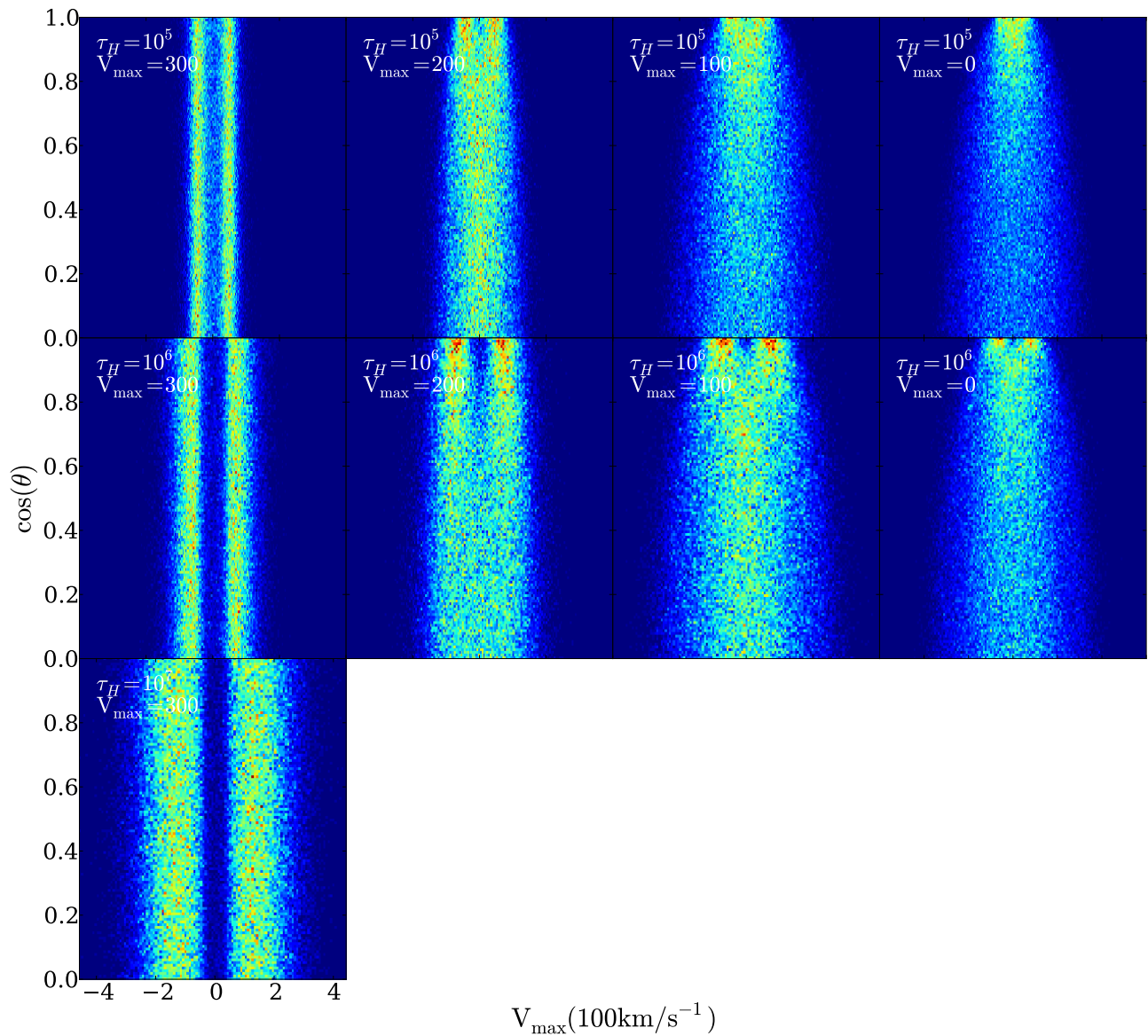
FIG. 3.— Same as Figure 2 for Lyα photons initialized homogeneously throughout the sphere.

$\tau_{\rm H}$, dust optical depth $\tau_{\rm a}$ and the bulk velocity field $\vec{v}$. Our codes treat the gas as homogeneous in density ($\tau_{\rm H}$, $\tau_{\rm a}$) and temperature.

2.3. Grid of Simulated Galaxies

In the Monte Carlo calculations we follow the propagation of $N_\gamma = 10^5$ numerical photons through different spherical galaxies. For each galaxy we vary at least one of the following parameters: the maximum rotational velocity $V_{\rm max}$, the hydrogen optical depth τ_H, the dust optical depth τ_a and the initial distribution of photons with respect to the gas. There are 60 models initial combining all variations of the input parameters. Table 1 summarizes the different parameters.

Additionally, we have used two independently developed Monte Carlo codes (Forero-Romero et al. 2011; Dijkstra & Kramer 2012) to perform the calculations. The results we report are robust in the sense that they are obtained by both codes.

Physical Parameter (units)	Symbol	Values
Velocity (km s^{-1})	$V_{\rm max}$	0, 50, 100, 200, 300
Hydrogen Optical Depth	τ_H	10^5, 10^6, 10^7
Dust Optical Depth	τ_a	0,1
Photons Distributions		Central, Homogeneous

TABLE 1
SUMMARY OF PHYSICAL PARAMETERS OF OUR MONTE CARLO
SIMULATIONS.

3. RESULTS

The central result of this paper are summarized in Figures 2 and 3. They show 2D histograms of the escape frequency x and outgoing angle θ parameterized by $|\mu|$. Constructing the emission line with photons around a value of μ would gives us the emission detected by an observer located at an angle θ with respect to the rotation axis. We have veryfied that the solutions are indeed symmetric with respect to $\mu = 0$.
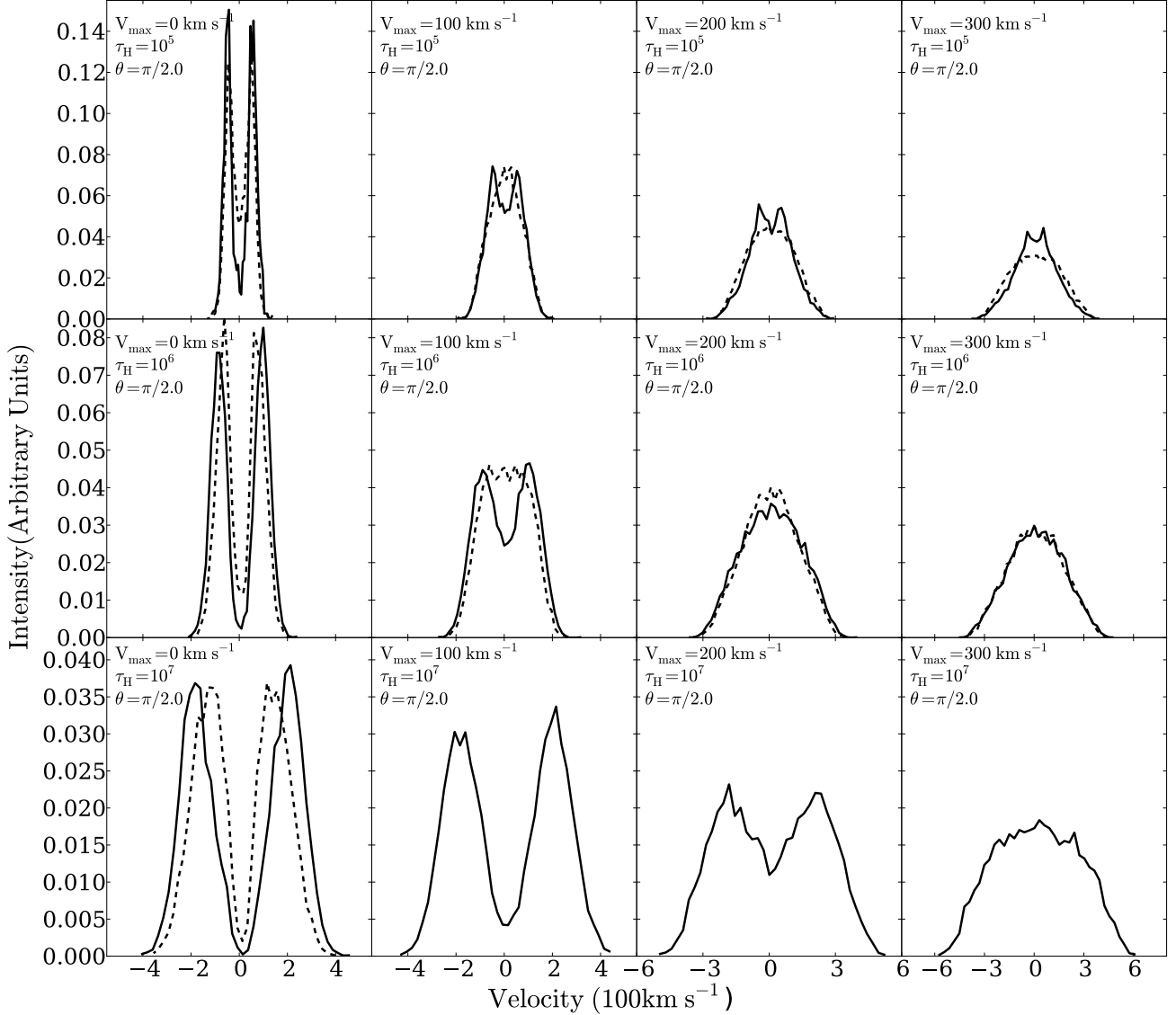
FIG. 4.— Shape of the Lyα line for different maximum rotational velocities for a LoS perpendicular to the rotation axis ($|\mu| \sim 0$). The continuous (dashed) line represents the central (homogeneous) source distributions. The panels follow the same distribution as in Figures 2 and 3.

From these Figures we can see that the line properties change with rotational velocity and depend on the viewing angle θ. In the next subsections we describe in detail the changes of the morphology with velocity, optical depth and viewing angle. We characterize the line morphology by its total intensity, the full width at half maximum (FWHM) and the location of the peak maxima. In order to interpret the morphological changes in the line we also report the median number of scatter for each Lyα photon in the simulation. For the models where dust is included we measure the escape fraction as a function of rotational velocity.

3.1. *Line Morphology*

The first column in both Figures 2 and 3 shows that for the static sphere the line properties are independent of $|\mu|$, as it is expected due to the spherical symmetry. However, for increasing rotational velocities, at a fixed optical depth, there are clear signs that this symmetry is broken.

If the viewing angle is aligned witht the rotation axis, $|\mu| \sim 1$, the Lyα line keeps a double peak with minor changes with increasing rotational velocity. However, for a line of sight perpendicular to the rotation axis, $|\mu| \sim 0$, the impact of rotation is larger. This is clear in Figure 4 where we present the different line morphologies for $|\mu| \sim 0$ for both the homogeneous and central configurations. The panels have the same distribution as Figures 2 and 3.

In the case of $|\mu| \sim 0$ there are three clear effects on the line morphology as the rotational velocity increases. First, the line broadens; second, the double peaks reduce their intensity; and third, the intensity at the line center rises. The last two effects merge to give the impression that the double peaks are merged into one at high rotational velocities, a result that is evident for the homogeneously distributed sources as shown in the dashed lines of Figure 4.
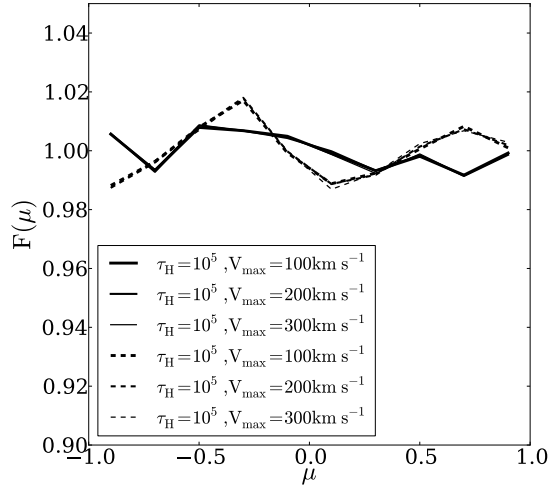
FIG. 5.— Integrated flux distribution as a function of the viewing angle as parameterized by μ. Continous (dashed) correspond to central (homogeneous) source distribution. The models correspond to an optical depth of $\tau_H = 10^5$ and rotational velocities of $100\,\mathrm{km\,s^{-1}}$, $200\,\mathrm{km\,s^{-1}}$ and $300\,\mathrm{km\,s^{-1}}$. The distributions are flat in the range of models probed in this paper, meaning that the integrated flux for all viewing angles is the same.

3.2. *Integrated Line Intensity*

Besides the change in morphology, we now consider possible variations in the integrated flux with respect to the viewing angle θ. We define the normalized flux seen by an observer at an angle μ by:

$$F(\mu) = \frac{2\Delta N}{N \Delta \mu}, \qquad (4)$$

where $\mu = \cos\Theta$, N is the total number of outgoing photons, ΔN is the number of photons in an angular bin $\Delta\Theta$. This definition satisfies the condition $\int_{-1}^{1} F(\mu)d\mu/2 = 1$. In the case of perfect spherical simmetry one expects a flat distribution of $F(\mu) = 1$.

Figure 5 shows the results for a selection of models with $\tau_H = 10^5$, different rotational velocities and both for the central and homogeneous source distributions. The distributions do not show any trend, beyond some fluctuations below the 2% level.

This is a remarkable result. In spite of that the rotation axis defines preferential direction, the integrated flux is the same for all viewing angles, at least for the range of parameters explored in this paper.

3.3. *Full Width at Half Maximum*

We use the full width at half maximum (FWHM) to quantify the line broadening. We measure this width from the velocity histogram by finding the values of the velocities at half maximum intensity. We use lineal interpolation between histogram points to get a value more precise than the bin size used to construct the line intensity.

Figure 6 shows the FWHM for all models as a function of the viewing angle. The FWHM increases for decreasing values of μ and increasing values of $V_{\max}$. In Figure **??** we fix $|\mu| < 0.1$, i.e. viewing angle perpendicular to the rotation axis, and plot the FWHM as a function of rotational velocity.

Source Distribution	τ_H	$V_{\max}$ (km s^{-1})				
		0	50	100	200	300
Homogeneous	10^5	0.263	0.266	0.309	0.357	0.370
	10^6	0.289	0.289	0.309	0.360	0.393
	10^7	0.227	0.229	0.231	0.254	0.281
Central	10^5	0.096	0.097	0.096	0.096	0.096
	10^6	0.066	0.066	0.066	0.066	0.066
	10^7	0.015	0.016	0.016	0.016	0.015

TABLE 2
ESCAPE FRACTION VALUES FOR ALL DUSTY MODELS.

we parametrize the dependency of the line width with $V_{\max}$ as

$$\mathrm{FWHM}^2 = \mathrm{FWHM}_0^2 + V_{\max}^2/\lambda^2, \qquad (5)$$

where FWHM_0 is the velocity width in the static case and λ is a positive scalar to be determined as a fit to the data. With this test we want to know to what extent the new velocity width can be expressed as a quadratic sum of the two relevant velocities in the problem. That all the models fall into two families of straight lines, for central and homogeneously emitted sources, justifies this choice of parameterization.

We fit simultaneously all the points corresponding to each one of this families to find $\lambda_c = 0.84 \pm 0.06$ and $\lambda_h = 0.54 \pm 0.10$ respectively.

3.4. *Line Maxima*

We measure the peak maxima position to quantify the transition from double into single peak profiles. We do this as a function of the viewing angle θ for different rotational velocities. The results are summarized in Figure 8. There are two interesting features that deserve attention. First, for a viewing angle parallel to the rotational axis ($\mu \sim 1.0$) the maxima of all models are similar regardless of the rotational velocity. Second, at a viewing angle perpendicular to the rotation axis ($\mu \sim 0.0$) a good fraction of models become single peaked. This feature appears more frequently for homogeneously distributed sources if all the other parameters are equal.

3.5. *Dusty Clouds: Escape Fraction*

We now estimate the escape fraction f_{esc} for the dusty models. The main result is that we do not find any dependence with the viewing angle but there is a strong dependence with the rotational velocity for the homogeneous models.

The left panel in Figure 9 summarizes the findings about the dependence with the rotational velocity. The left panel shows the escape fraction as a function of the rotational velocity. To construct this Figure we take into account all the photons regardless of its outgoing direction. We observe that the curves for the central source distribution stay flat, while for the homogeneous case there is a clear rise with rotational velocity. Rotation has a higher relative impact in the models with low optical depth. For instance, in models with $\tau_H = 10^5$, the static escape fraction is 0.26 and increases to 0.37 for $V_{\max} = 300$ km s^{-1}. Table 2 lists all the values for the escape fraction.

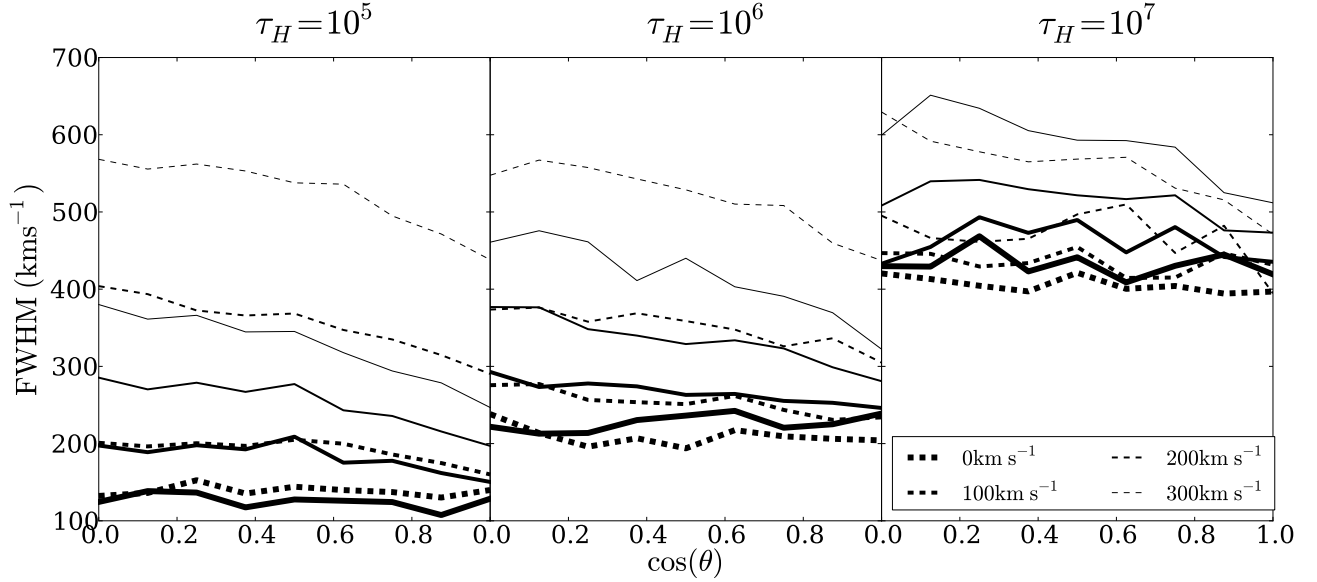In the right panel of Figure 9 we put these results in the context of the analytic solution for the infinite slab

FIG. 6.— FWHM for the non-dusty models as a function of the viewing angle parameterized by $|\cos\theta|$. Continuous (dashed) lines correspond to central (homogeneous) source distributions. The general trend is of an decreasing line width as the line of sight becomes parallel to the rotation axis.
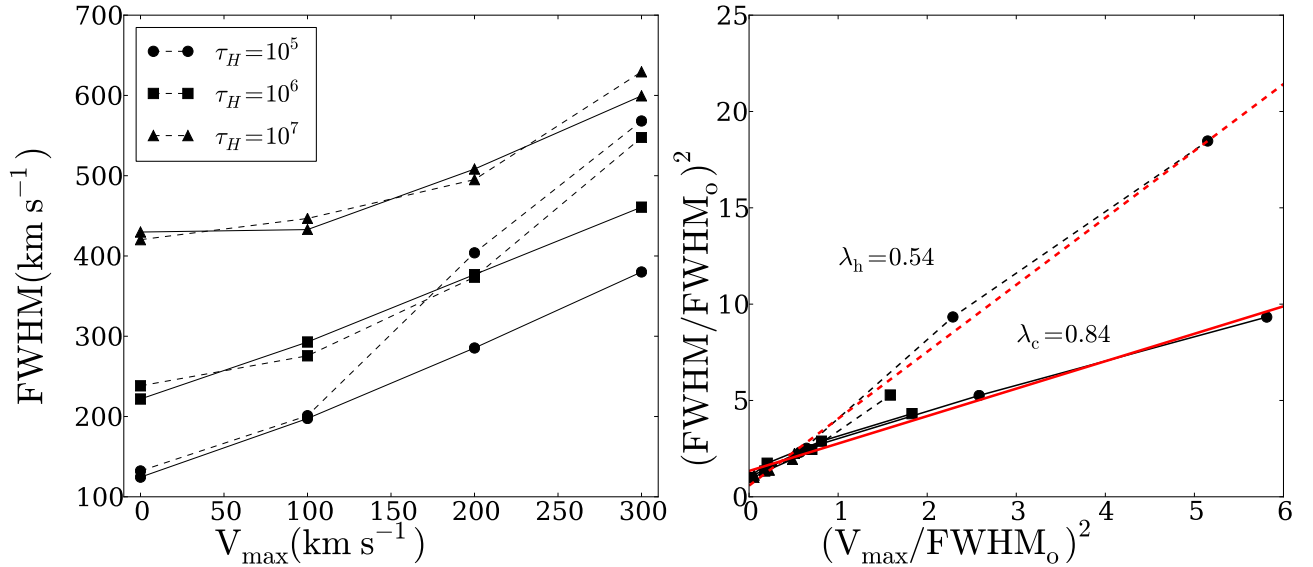

FIG. 7.— FWHM for the non-dusty models as a function of rotational velocity $V_{\max}$. The left panel shows the results in velocity units while the right panel normalizes the data by the FWHM in the static case. Continuous (dashed) lines correspond to central (homogeneous) source distributions. The straight lines represent the fit to the data using the expression in Eq. (5).

(Neufeld 1990). In Neufeld's set-up the analytic solution depends uniquely on the product $(a\tau_{\rm H})^{1/3}\tau_A$ where $\tau_A = (1 - A)\tau_a$, valid only in the limit $a\tau_{\rm H} \gg 1$. The dashed lines in the right panel of Figure 9 show the results for the different rotational velocities for the homogeneous models. First of all we note that the escape fraction increases slightly from $\tau_{\rm H} = 10^5$ to $\tau_{\rm H} = 10^6$, which is counterintuitive as we expected that increasing $\tau_{\rm H}$ requires more scattering before the photon escapes, which would increase the probability that photons are destroyed by dust.

However, this naive interpretation is incorrect: increasing $\tau_{\rm H}$ from 10^5 to 10^6 causes us to transition from the 'optically thick' to the 'extremely optically thick' regime. In the optically thick regime, Lya photons can escape in 'single flight' which corresponds to a scenario in which the photon resonantly scatters $10^4 - 10^5$ times until it is scattered into the wing of the line ($x \sim 3 - 4$). At these frequencies the medium is optically thin, and the photons can escape efficiently in a single flight. In contrast, in an extremely optically thick medium Lyα photons escape in a 'single excursion' (Adams 1972). Here, photons that are scattered into the wing of the line escape from the medium in a sequence of wing scattering events. In both cases, Lyα photons resonantly scatter 10^4-10^5 times. Because we keep our clouds the same size, the mean free
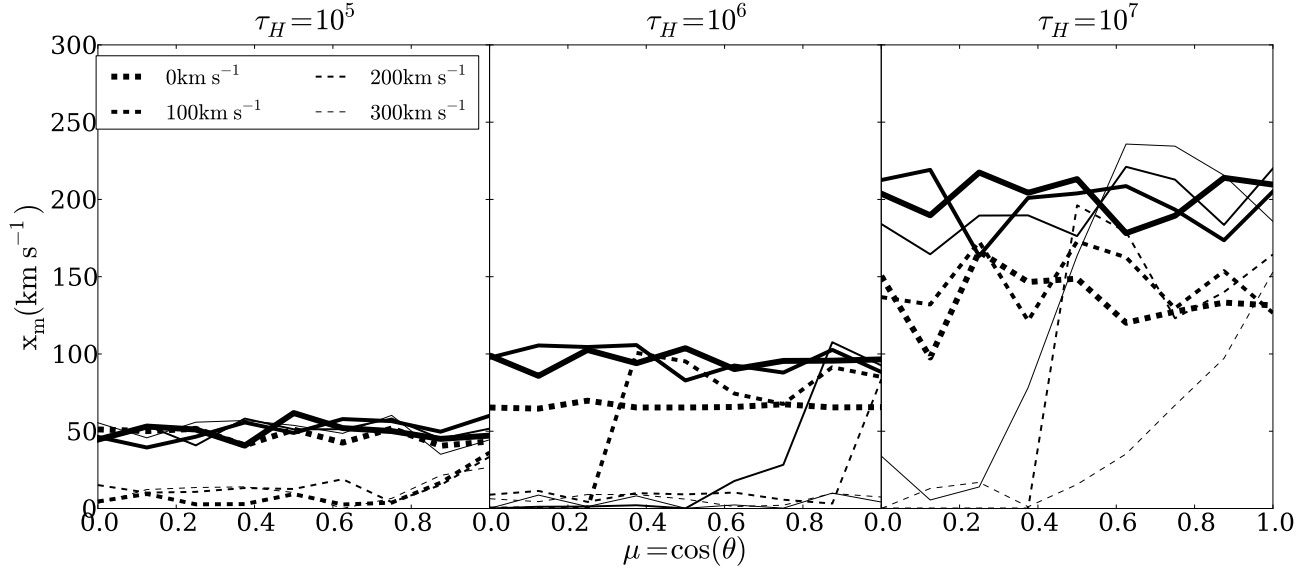
FIG. 8.— Position of the line maxima as a function of maximum rotational velocity V_{max}. Continuous (dashed) lines correspond to central (homogeneous) source distributions. A value of $x_{max} = 0$ indicates that line becomes single peaked.
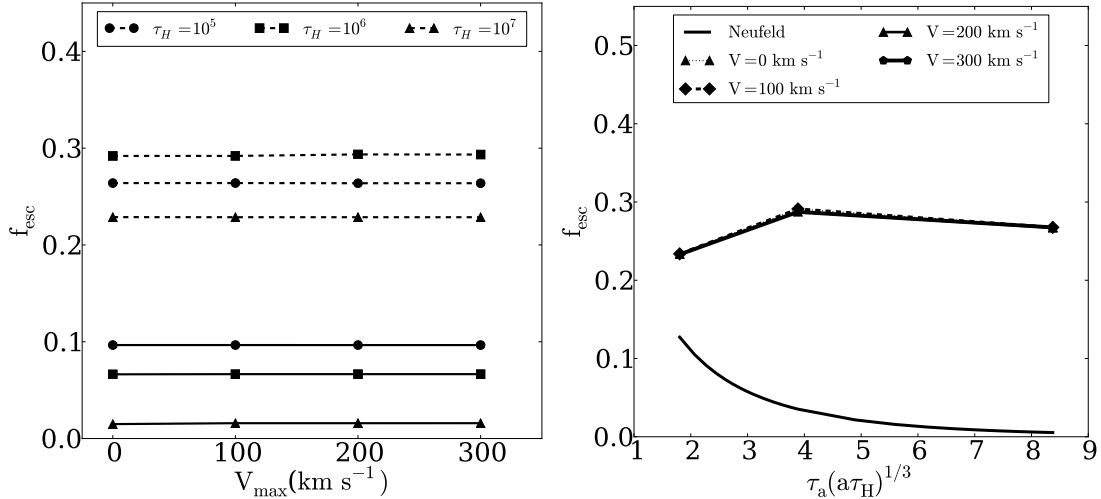

FIG. 9.— Effects of rotation on the escape fraction. Left panel, escape fraction as a function of rotational velocity. All these models have $\tau_a = 1$. The continuous (dashed) lines correspond to central (homogeneous) models. Right panel, escape fraction as a function of the product $(a\tau_H)^{1/3}\tau_A$. The analytic solution for the infinite slab is shown as a continuous line. Different lines correspond to different rotational velocities for the homogeneous models.

path of Lya photons that scatter resonantly is 10 times larger for the case $\tau_H = 10^5$ than for $\tau_H = 10^6$. If we compute the average distance D travelled by Lyα photons through a medium of size R as a function of line center optical depth τ_H, then we find that during the transition from optically thick to extremely optically thick the mean traversed distance D actually decreases slightly. This decrease is unique to this transition region, and D generally increases with τ_H at other values of τ_H.

3.6. *Average Number of Scatterings*

The number of scatterings affects the escape frequency of a Lyα photon. Studying this quantity can help us in claryfing two results that we have observed for homogeneous models in the previous sections: the quick emergence of a single peak and the increase in the es-

cape fraction.

A possible explanation for these two results is that some photons close to the surface can escape with a low number of scatterings. This has a two consequences: the escaping photons do not have time to scatter away from the line's center and also have less chances to find an absorbing dust grain.

In Figure 10 we show the average number of scatterings $\langle N_{scatt} \rangle$ as a function of the cosinus of the outgoing angle $|\cos\theta|$ and the rotational velocity V_{max}. From the right panel observe that the number of scatterings and the outgoing angle are independent. This plot corresponds to the specific case of the central model with $\tau = 10^5$ and $V_{max} = 300\,\text{km s}^{-1}$, but we have veryfied that this holds for all models. This allows us to construct statistics
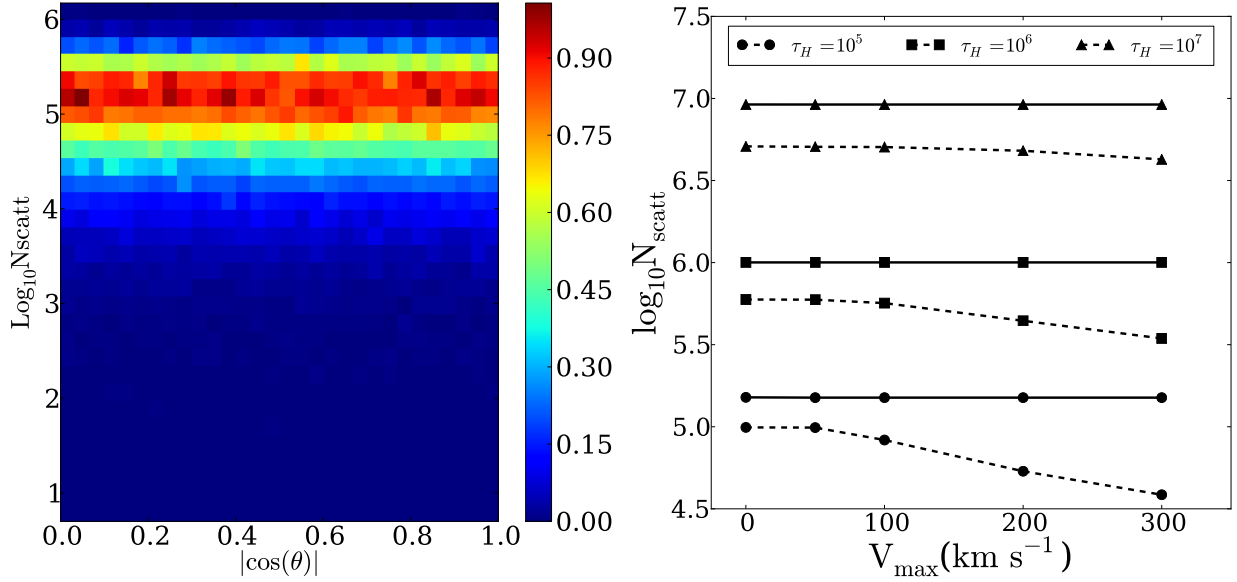
FIG. 10.— Logarithm of the average number of scatterings as function of μ (left panel) and the maximum rotational velocity V_{max}. The left panel shows the behaviour for $\tau = 10^5$ and $V_{max} = 300\,\mathrm{km\,s^{-1}}$ as a function of $|\cos\theta|$; the independence of N_{scatt} with μ is present in all models. In the right panel the continuous (dashed) lines represent an central (homogeneous) distribution of sources; there is a clear decrease in the number of scatterings for the homogenously distributed sources.

using all the outgoing photons regardless of their value of $\cos\theta$.

The right panel of Figure 10 shows how the average number of scatterings decreases for larger rotational velocities in the case of homogeneous source distributions. For instance, for $\tau_{\mathrm{H}} = 10^5$ the average number of scatterings decreases by 61% at $V_{\mathrm{max}} = 300\,\mathrm{km\,s^{-1}}$ in comparison to the static case. For the central source distribution the average number of scatterings $\langle N_{\mathrm{scatt}}\rangle$ changes less than 0.5%.

In order to gain a deeper understanding of these results we make 2D histograms for the number of scatterings as a function of the outgoing dimensionless frequency x. In Figure 11 we show these results in the case $\tau_{\mathrm{H}} = 10^5$ for the static case and $V_{\mathrm{max}} = 300\,\mathrm{km\,s^{-1}}$. The upper (lower) panels show the results for the homogeneous (central) source distribution. The color scale is logarithmic in the number of photons at a certain value $x - N_{\mathrm{scatt}}$.

The top right panel of Figure 11 (homogeneous sources, high rotational velocity) supports our hypothesis about the photo-sphere in the homogeneous distribution. In this case most of the photons that left with $x \sim 0$ have escaped with less than 10 scatterings. This also explains the decrease in the average number of scatterings observed in Figure 10. We have also veryfied that these photons are indeed emitted closer to the surface than to the center of the sphere.

However, for a central distribution the situation is quite different (lower panels in Figure 11). In this case the number of scatterings remains high, in the order of the optical depth, but the two peaks do get closer to each other. The most probable physical picture is that each scattering, due to the bulk velocity of the gas, is inefficient in driving the photon outside the line center.

We now proceed with a more detailed quantification of the number of scatterings in our simulations. We guide the measurement by the fact that in static cases, a large

value of the optical depth correlates with a high number of scatterings. This has been precisely quantified in the case of static infinite slab. In this model for centrally emitted sources the average number of scatterings depends only on the optical depth $\langle N_{\mathrm{scatt}}\rangle = 1.612\tau_{\mathrm{H}}$ (Adams 1972; Harrington 1973), for homogeneously distributed sources $\langle N_{\mathrm{scatt}}\rangle = 1.16\tau_{\mathrm{H}}$ (Harrington 1973).

We perform a similar quantification of in our speherical setup for the static spheres. We find that for the central model the number of scatterings is proportional to the optical depth, with $\langle N_{\mathrm{scatt}}\rangle = (1.50, 1.00, 0.92)\tau_{\mathrm{H}}$ for optical depth values of $\tau_{\mathrm{H}} = (10^5, 10^6, 10^7)$ respectively. For the homogeneous static sphere we find that $\langle N_{\mathrm{scatt}}\rangle = (0.99, 0.59, 0.51)\tau_{\mathrm{H}}$, this represents factors of $(0.66, 0.59, 0.55)$ lower than the centrally emitted photons.

For the homogeneous rotating sphere at $V_{\mathrm{max}} = 300\,\mathrm{km\,s^{-1}}$ we find that $\langle N_{\mathrm{scatt}}\rangle = (0.38, 0.34, 0.42)\tau_{\mathrm{H}}$ which represents factors of $(0.26, 0.34, 0.46)$ lower than the corresponding central case.

4. DISCUSSION

We now compare our findings to other computational results and discuss its possible implications for the interpretation of observational data.

Galaxy simulations with gas rotation. Verhamme et al. (2012) studied Lyα line emission in two high resolution simulations of individual galaxies. The main purpose of their study was to assess the impact of two different Inter-Stellar Medium (ISM) prescriptions. However, each simulated galaxy had a disc structure with a clear rotation pattern in the ISM and inflowing gas from the circum-galactic region. The configuration had an axial symmetry and they reported a strong dependence of both the escape fraction and the total line intensity as a function of the θ angle. In our results, none of these two quantities has a dependence either on the inclination angle or the rotational velocity. We suggest that he
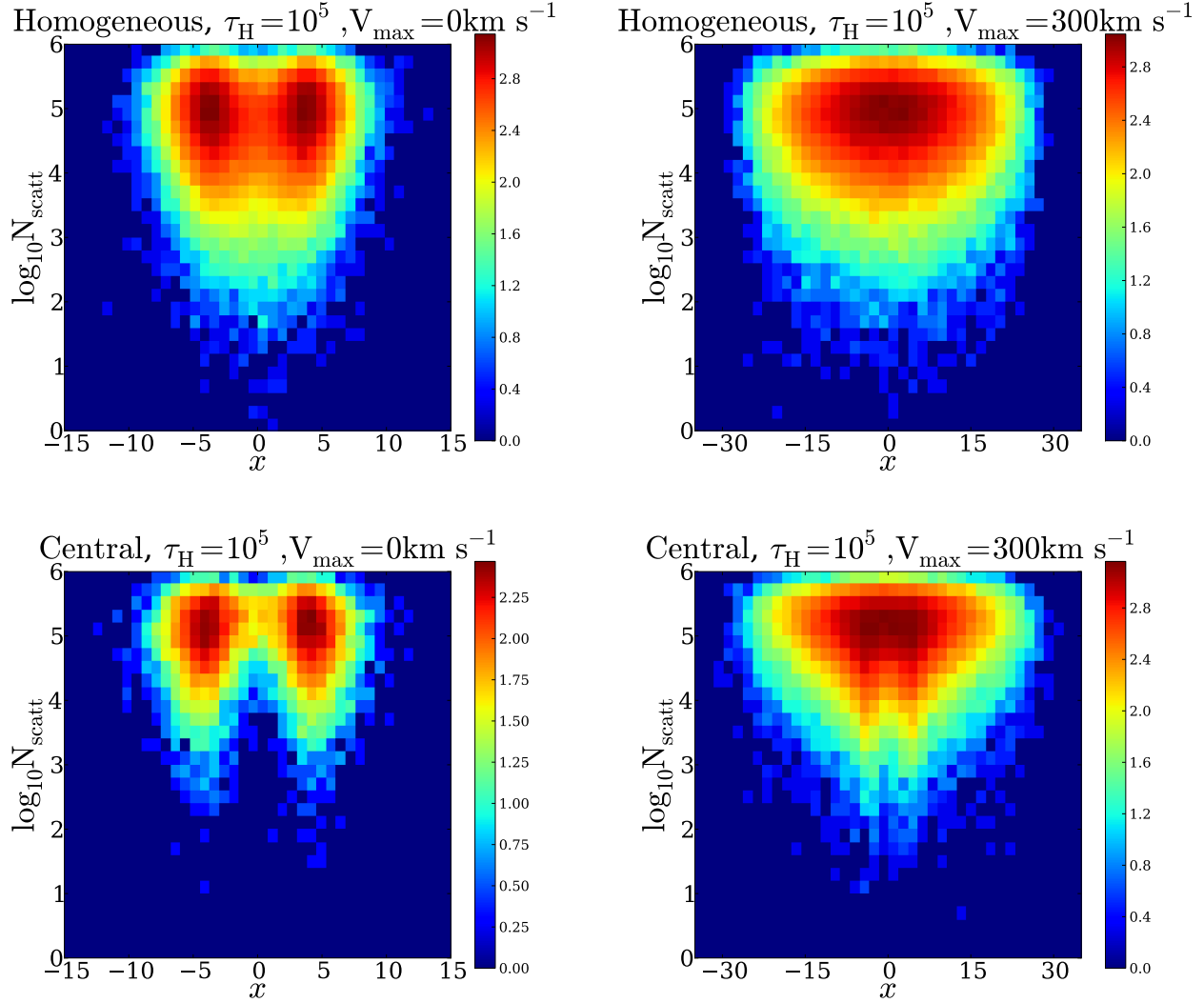
Fig. 11.— 2D histogram of N_{scatt} vs x. The upper (lower) panels show the homogeneous (central) source distribution. Left panels corresponds to the static case and right panels correspond to $V_{\mathrm{max}} = 300\,\mathrm{km\,s^{-1}}$. The color scale is logarithmic on the number of photons with given values of N_{scatt} and x. . A results that stands out is in the upper right panel, showing that in homogeneously distributed sources a large number of photons can escape escape after a few scatterings, $N_{\mathrm{scatt}} < 10$.

effect reported by Verhamme et al. (2012) is consistent with being a consequence of the different hydrogen optical depth for different viewing angles and not as an effect of the bulk rotation.

Single peaked lines. The presence of single peaked profiles has been associated to inflow/outflow dynamics (Verhamme et al. 2006; Dijkstra & Kramer 2012). In this paper we show that gas bulk rotation can also be considered as a probable origin for that behavior, provided that the observed single peak is highly symmetric. Similarly, in the case of double peaked lines with a high level of flux at the line center, rotation also deserves to be considered in the pool of possible bulk flows responsible for that feature, specially if the two peaks have similar intensities. This highlights that in order to interpret the observations of Lyα emitting galaxies it is necessary to consider the possible effect of different inclination angles along the line of sight.

Systemic velocities. There are observational measurements for the velocity shift between the Lyα and other emission lines. In our study we find that the position of the peak maxima is insensitive to the rotational velocity of the gas. In our model the only parameter that can influence the peak maxima position is the optical depth.

Anisotropic emission. In our studies the integrated flux is constant is independent of the viewing angle. This rules out the possibility of having an observational indication of gas bulk rotation from measurements of the line equivalent width. A possible way to obtain an anisotropic flux with the same gas configuration is to allow for anisotropic emission (Zheng & Wallace 2013; Behrens et al. 2014). We explore these scenarios in future work (Remolina-Gutierrez et al., in prep.).

Additional uncertainty on the Lyα escape fraction. Study of high redshift LAEs in numerical simulation often requires the estimation of the Lyα escape

fraction in order to compare their results against observations (Forero-Romero et al. 2011; **?**, 2012; Orsi et al. 2012; Garel et al. 2012). Most of these models estimate the escape fraction from the column density of dust and neutral Hydrogen. The results of our simulation suggest that the rotational velocity has also to be accounted for, having an impact on the values of the escape fractions by factors of ~ 2.

5. CONCLUSIONS

In this paper we quantified for the first time in the literature the effects of gas bulk rotation in the morphology of the Lyα emission line in star forming galaxies. Our results are based on the study of an homogeneous sphere of gas with solid body rotation. We explore a range of models by varying the rotational speed, hydrogen optical depth, dust optical depth and initial distribution of Lyα photons with respect to the gas density. As a cross-validation, we obtained our results from two independently developed Monte-Carlo radiative transfer codes.

Two conclusions stand out from our study. First, rotation clearly impacts the Lyα line morphology; the width and the relative intensity of the center of the line and its peaks are affected. Second, rotation introduces an anisotropy for different viewing angles. For viewing angles close to the poles the line is double peaked and it makes a transition to a single peaked line for high rotational velocities and viewing angles along the equator. This trend is clearer for spheres with homogeneously distributed radiation sources than it is for central sources.

Remarkably, we find two quantities that are invariant with respect to the viewing angle and the rotational velocity: the integrated flux and the escape fraction. The exception is the models with homogeneously distributed sources, which present an escape fraction dependent on the rotational velocity, but still independent of the viewing angle. We showed that these results could be interpreted in terms of the average number of scatterings for the photons.

Quantitatively, the main results of our study are summarized as follows.

- In all of our models, rotation induces changes in the line morphology for different values of the angle between the rotation axis and the LoS, θ. The changes are such that for $\cos\theta \equiv \mu \sim 0$, i.e. LoS perpendicular to the rotation axis, and high rotational velocities the line becomes single peaked.

- For a viewing angle with $\mu = 0$ the line width increases with rotational velocity. This change approximately follows the functional form $\mathrm{FWHM}^2 = \mathrm{FWHM}_0^2 + (V_{\max}/\lambda)^2$, where FWHM_0 indicates the line width for the static case and λ is a constant. We have determined this constant to be $\lambda_{\mathrm{c}} = 0.84 \pm 0.06$ and $\lambda_{\mathrm{h}} = 0.54 \pm 0.10$ for the central and homogeneous source distributions, respectively.

- At fixed rotational velocity the line width decreases as $|\mu|$ increases, i.e. the smallest value of the line width is observed for a line of sight parallel to the ration axis. However the lowest values are always larger than the values for the static case.
- The single peaked line emerges for homogeneously distributed sources when the rotational velocity is larger than half FWHM_0 and $\mu \sim 1$.

- For central sources we find that the escape fraction does not change with rotational velocity nor with the viewing angle. We interpret this in terms of the average number of scatterings which does not significantly change with rotation. This is due to the fact that the vast majority of scatterings events are resonant, during which the mean free path is very short and the effect of gas bulk rotation is not enough to affect Lyα photons.

- For homogeneous sources we find that the as rotational velocity increases, the escape fraction rises by a factor of ~ 2 with respect to the static situation. We also interpret this change in terms of the average number of scatterings. In the second part of §3.3 we show that the average number of scatterings decreases a 40% compared to the static case, while a large fraction of photons escape with less than 10 scatterings.

Comparing our results with recent observed LAEs we find that many morphological features such as high central line flux, single peak profiles could be explained by gas bulk rotation present in these LAEs.

The definitive and clear impact of rotation on the Lyα morphology suggests that this is an effect that should be taken into accunt at the moment of interpreting high resolution spectroscopic data. To this end, we defer a discussion of observed lines features in the context of gas bulk rotation to a future publication (Remolina-Gutierrez et al., in prep.).

APPENDIX

ANALYTIC EXPRESSION FOR LYα SPECTRUM EMERGING FROM ROTATING CLOUD

Lyα scattering through a an optically thick gas cloud that is undergoing solid-body rotation (i.e. the angular speed around the rotation axis is identical for each hydrogen atom) proceeds identical as in a static cloud. While scattering events off atoms within the rotating cloud impart Doppler boosts on the Lyα photon, these Doppler boost are only there in the lab-frame. In the frame of the rotating gas cloud, all atoms are stationary w.r.t each other, and the scattering process proceeds identical as in the static case[1]. This explains why the escape fraction of Lyα photon is independent of the rotation velocity off the cloud, irrespective of the rotation speed.

The spectrum emerging of photons emerging from a rotating gas cloud is also identical as for the static case in a frame that is co-rotating with the cloud. However, the surface of cloud now moves in the lab-frame. Each surface-element on the rotating cloud now has a bulk velocity w.r.t a distant observer. In order to compute the spectrum emerging from this rotation cloud, we have to sum over all surface elements (weighted by their intensity).

To provide an analytic description of this emerging spectrum, we adopt the geometry shown in Fig 1 (note this differs slightly from the main body of the paper. My 'observer' sits along the x-axis. I think yours sits along the z-axis. We have to makes sure this is done consistently throughout the paper). The sightline to the observer & rotation define
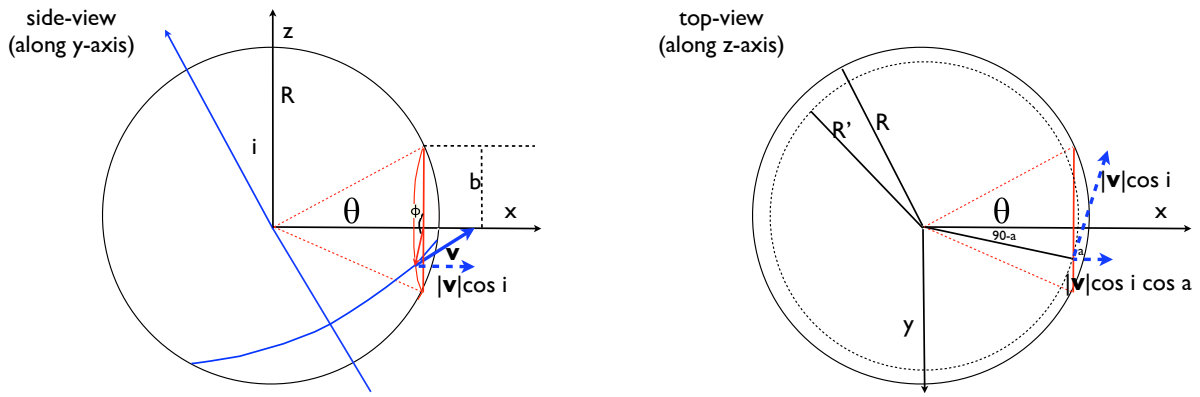

FIG. 12.— Adopted geometry for evaluating the analytic spectrum.

the $x - z$ plane. The observer sits along the axis. The *left panel* in Fig 1 shows the view from the $y - axis$. The rotation axis makes an angle i with respect to the z-axis. We sum up spectra from individual patches by integrating over the impact parameter b, and angle ϕ. Each (b, ϕ) corresponds to a point on the sphere. This point has a velocity vector $\mathbf{v}(b, \phi, i)$, which we denote with $\mathbf{v}$ for brevity.

$$J(x, i) = 2\pi \int_0^R db\, b \int_0^{2\pi} d\phi\, S(b, \phi) J(x, b, \phi, i) \approx 2\pi \int_0^R db\, b \int_0^{2\pi} d\phi\, J(x, b, \phi, i)$$

$$J(x, b, \phi, i) = \frac{\sqrt{\pi}}{\sqrt{24} a \tau_0} \left(\frac{(x - x_b)^2}{1 + \cosh\left[\sqrt{\frac{2\pi^3}{27}} \frac{|(x - x_b)^3|}{a \tau_0} \right]} \right)$$

The velocity v_b is the component of $\mathbf{v}$ projected onto the line-of-sight. This component is given by

$$v_b(b, \phi, i) = v_{\rm rot} \sqrt{1 - (b/R)^2 \cos^2 \phi}\, \cos i\, \sin \beta \tag{A1}$$

$$\tan \beta = \frac{b \sin \phi}{\sqrt{R^2 - b^2}}. \tag{A2}$$

The quantity $S(b, \phi)$ denotes the surface brightness of the sphere at (b, ϕ). We have assumed in our analytic calculations that $S(b, \phi)$ is constant. The assumption $S(b, \phi) = {\rm constant}$ corresponds to $I(\mu) \propto \mu$ at the surface, where μ denotes the cosine of the angle of the propagation direction of the outgoing photon and the normal to the spheres surface: a fixed db corresponds to a physical length $ds = db/\mu$ on the sphere. If $I(\mu)$ were constant, this would imply that the sphere should appear brighter per unit b. A constant surface brightness profile requires the directional dependence for

---

[1] An alternative - more quantitative way - to view this is to consider the path of an individual photon: say the photon travels a distance corresponding to $\tau = 1$, scatters by 90 degrees, then travels another distance corresponding to $\tau = 1$. It is easy to show that the point where the photon ends up is independent of the assumed rotation velocity of the cloud.

$I(\mu) \propto \mu$ to correct for this. Indeed, this is what is expected for the escape of Lyα photons from static, extremely opaque media (see Ahn, Lee & Lee, 2001; their Fig 4 and accompanying discussion).

It is worth stressing that the analytic calculation is clearly not a complete analytic calculation, and we do not expect perfect agreement: we *assumed* a functional form for the surface brightness profile [or for $I(\mu)$]. It is important to realise that $I(\mu)$ itself may depend on the spectrum. I.e., analytic solutions exist for $J(x) = \int_0^1 I(x,\mu)d\mu$ at the boundary, and *approximate* expressions for $I(\mu) = \int dx I(x,\mu)$, but none for $I(x,\mu)$ itself.

Fig 2 shows some examples of analytic vs. full MC spectra. The area under all spectra are normalised to 1. The MC simulations used 10^5 photons. The two methods clearly give good agreement, though not perfect. In particular, Fig 3 shows that the MC gives rise to a spectrum that is slightly more concentrated to the centre. It is easy to get better agreement my modifying the surface brightness profile (e.g. if $S(b) = 2 - b$, then the analytic calculation agrees better) In any case, the analytic calculation closely captures the results obtained from the full calculations from the MC simulations. As such, they are extremely useful & provide us with a quick tool to verify our calculations at the first order level.

REFERENCES

Adams, T. F. 1972, ApJ, 174, 439
Ahn, S.-H., Lee, H.-W., & Lee, H. M. 2000, Journal of Korean Astronomical Society, 33, 29
—. 2001, ApJ, 554, 604
Ahn, S.-h., Lee, H.-w., & Lee, H. M. 2014, 000
Auer, L. H. 1968, ApJ, 153, 783
Avery, L. W., & House, L. L. 1968, ApJ, 152, 493
Barnes, L. A., Haehnelt, M. G., Tescari, E., & Viel, M. 2011, MNRAS, 416, 1723
Behrens, C., Dijkstra, M., & Niemeyer, J. C. 2014, A&A, 563, A77
Behrens, C., & Niemeyer, J. 2013, A&A, 556, A5
Chonis, T. S., Blanc, G. A., Hill, G. J., Adams, J. J., Finkelstein, S. L., Gebhardt, K., Kollmeier, J. A., Ciardullo, R., Drory, N., Gronwall, C., Hagen, A., Overzier, R. A., Song, M., & Zeimann, G. R. 2013, ApJ, 775, 99
Dijkstra, M., Haiman, Z., & Spaans, M. 2006, ApJ, 649, 14
Dijkstra, M., & Kramer, R. 2012, MNRAS, 424, 1672
Finkelstein, S. L., Papovich, C., Dickinson, M., Song, M., Tilvi, V., Koekemoer, a. M., Finkelstein, K. D., Mobasher, B., Ferguson, H. C., Giavalisco, M., Reddy, N., Ashby, M. L. N., Dekel, a., Fazio, G. G., Fontana, a., Grogin, N. a., Huang, J.-S., Kocevski, D., Rafelski, M., Weiner, B. J., & Willner, S. P. 2013, Nature, 502, 524
Forero-Romero, J. E., Yepes, G., Gottlöber, S., Knollmann, S. R., Cuesta, A. J., & Prada, F. 2011, MNRAS, 415, 3666
Forero-Romero, J. E., Yepes, G., Gottlöber, S., & Prada, F. 2012, MNRAS, 419, 952
Garel, T., Blaizot, J., Guiderdoni, B., Schaerer, D., Verhamme, A., & Hayes, M. 2012, MNRAS, 422, 310
Gawiser, E., Francke, H., Lai, K., Schawinski, K., Gronwall, C., Ciardullo, R., Quadri, R., Orsi, A., Barrientos, L. F., Blanc, G. A., Fazio, G., & Feldmeier, J. J. 2007, ApJ, 671, 278
Hansen, M., & Oh, S. P. 2006, MNRAS, 367, 979
Harrington, J. P. 1973, MNRAS, 162, 43

Hunter, J. D. 2007, Computing In Science & Engineering, 9, 90
Koehler, R. S., Schuecker, P., & Gebhardt, K. 2007, A&A, 462, 7
Kulas, K. R., Shapley, A. E., Kollmeier, J. A., Zheng, Z., Steidel, C. C., & Hainline, K. N. 2012, ApJ, 745, 33
Laursen, P., Sommer-Larsen, J., & Andersen, A. C. 2009, ApJ, 704, 1640
Loeb, A., & Rybicki, G. B. 1999, ApJ, 524, 527
Neufeld, D. A. 1990, ApJ, 350, 216
Orsi, A., Lacey, C. G., & Baugh, C. M. 2012, MNRAS, 425, 87
Ouchi, M., Shimasaku, K., Akiyama, M., Simpson, C., Saito, T., Ueda, Y., Furusawa, H., Sekiguchi, K., Yamada, T., Kodama, T., Kashikawa, N., Okamura, S., Iye, M., Takata, T., Yoshida, M., & Yoshida, M. 2008, ApJS, 176, 301
Partridge, R. B., & Peebles, P. J. E. 1967, ApJ, 147, 868
Pérez, F., & Granger, B. E. 2007, Computing in Science and Engineering, 9, 21
Rhoads, J. E., Malhotra, S., Dey, A., Stern, D., Spinrad, H., & Jannuzi, B. T. 2000, ApJ, 545, L85
Schenker, M. A., Stark, D. P., Ellis, R. S., Robertson, B. E., Dunlop, J. S., McLure, R. J., Kneib, J.-P., & Richard, J. 2012, ApJ, 744, 179
Verhamme, A., Dubois, Y., Blaizot, J., Garel, T., Bacon, R., Devriendt, J., Guiderdoni, B., & Slyz, A. 2012, A&A, 546, A111
Verhamme, A., Schaerer, D., Atek, H., & Tapken, C. 2008, 111, 89
Verhamme, A., Schaerer, D., & Maselli, A. 2006, A&A, 460, 397
Yajima, H., Li, Y., Zhu, Q., Abel, T., Gronwall, C., & Ciardullo, R. 2012, ApJ, 754, 118
Yamada, T., Nakamura, Y., Matsuda, Y., Hayashino, T., Yamauchi, R., Morimoto, N., Kousai, K., & Umemura, M. 2012, AJ, 143, 79
Zheng, Z., & Miralda-Escudé, J. 2002, ApJ, 578, 33
Zheng, Z., & Wallace, J. 2013, ArXiv e-prints